Electrodynamic and Excitonic Intertube Interactions in Semiconducting Carbon Nanotube Aggregates

Jared J. Crochet,[†,*] Jay D. Sau,[‡] Juan G. Duque,[†,§] Stephen K. Doorn,[†] and Marvin L. Cohen[⊥]

[†]Center for Integrated Nanotechnologies, Los Alamos National Laboratory, Los Alamos, New Mexico 87545, United States, [‡]Condensed Matter Theory Center and Joint Quantum Institute, University of Maryland, Baltimore, Maryland 20742, United States, [§]Chemistry Division, Physical Chemistry and Applied Spectroscopy Group, Los Alamos National Laboratory, Los Alamos, New Mexico 87545, United States, and [⊥]Department of Physics, University of California at Berkeley, and Materials Sciences Division, Lawrence Berkeley National Laboratory, Berkeley, California 94720, United States

ABSTRACT The optical properties of selectively aggregated, nearly single chirality single-wall carbon nanotubes were investigated by both continuous-wave and time-resolved spectroscopies. With reduced sample heterogeneities, we have resolved aggregation-dependent reductions of the excitation energy of the S_1 exciton and enhanced electron−hole pair absorption. Photoluminescence spectra revealed a spectral splitting of S_1 and simultaneous reductions of the emission efficiencies and nonradiative decay rates. The observed strong deviations from isolated tube behavior are accounted for by enhanced screening of the intratube Coulomb interactions, intertube exciton tunneling, and diffusion-driven exciton quenching. We also provide evidence that density gradient ultracentrifugation can be used to structurally sort single-wall carbon nanotubes by aggregate size as evident by a monotonic dependence of the aforementioned optical properties on buoyant density.

KEYWORDS: carbon nanotube bundles · exciton · delocalization · diffusion · spectroscopy · coherence · tunneling

The understanding of nanoscale charge and energy transfer phenomena is integral for the design of nanotechnology-inspired electro-optic devices.[1,2] In the past decade, there has been particular interest in nanoscale graphitic systems such as single-wall carbon nanotubes (SWNTs) and graphene because of their large aspect ratios, outstanding transport and mechanical properties, and high chemical stability.[3,4] Furthermore, it was recently shown that in both carbon nanotubes[5] and graphene[6] intriguing optical properties arise because of the screened Coulomb interaction between electrons and holes. Particularly, in carbon nanotubes, the optical spectra were found to be dominated by strongly bound Wannier-like excitons associated with each electron−hole pair sub-band.[7,8] Each subband exciton is known to have a C_2 inversion symmetry dictated fine structure associated with linear combinations of electron and hole wave functions from the K and K' valleys of the quantized graphene lattice.[9]

Spectroscopy has proven to be a powerful tool for investigating exciton dynamics in SWNTs.[10] Photoexcitations of the S_2 exciton (bright exciton of the E_{22} sub-band) were found to efficiently decay into the lower lying S_1 exciton (bright exciton of the E_{11} sub-band).[11] Subsequent decay of S_1 was found to be dominated by nonradiative processes, as evident from relatively low emission efficiencies of approximately 1%.[12] Moreover, recent reports of Förster intertube exciton energy transfer in aggregated tubes, colloquially referred to as bundles, of different chiralities have provided clues about the nature of intertube interactions.[13,14] However, in tube aggregates at van der Waals contact distances, dipolar coupling would most likely fail to describe exciton transfer because of the SWNT's nearly one-dimensional elongated structure.[15] This is supported by recent transient absorption experiments on ensembles of small SWNT aggregates where exciton transfer rates were found to exceed 100 ps^{-1}.[16] Mutual dielectric screening within an aggregate can also play an important role in altering isolated tube electronic properties. Transition energy red shifts of tens of millielectronvolts have been observed and ascribed to purely electrodynamic rather than direct excitonic intertube couplings.[17]

In this investigation, we find that the optical responses of aggregated SWNTs with the same chirality are strongly altered with respect to that of isolated tubes. Reductions in the S_1 exciton excitation energy with enhanced absorption from continuum states, reductions in the fluorescence quantum yield, and a spectral splitting of the S_1

* Address correspondence to jcrochet@lanl.gov.

Received for review September 27, 2010 and accepted February 25, 2011.

Published online March 10, 2011
10.1021/nn200427r

fluorescence suggest that both electrodynamic and excitonic intertube interactions are important for describing the optical properties of SWNT aggregates. However, exciton delocalization by intertube exciton tunneling is found to account for the majority of the observed deviations from isolated tube behavior. We also provide a general procedure for the self-assembly and structural sorting of well-defined SWNT aggregates which extends the capability of density differentiation of SWNTs by ultracentrifugation.[18]

RESULTS

Diameter enriched colloids of single-wall carbon nanotubes (SWeNT SG 65) were prepared by a cosurfactant variation of density gradient ultracentrifugation.[18] Analysis of the absorption spectra showed that ≈85% of the total (*n*,*m*) population was enriched in the (6,5) tube. Chirality enriched aggregates were prepared by placing 1 mL of (6,5) enriched tubes in a 35 kDa dialysis membrane submerged in a water bath. After 24 h, the suspension showed signs of flocculation and was resuspended in 2% sodium cholate by mild sonication.[19] The resuspended tubes were sorted by density gradient ultracentrifugation and revealed an isolated tube band followed by a broad aggregate band at larger densities (Figure 1a). The collected fraction's buoyant densities, ρ_b, were found to range from 1.055 to 1.148 g/cm^3. Average height profiles measured by atomic force microscopy (AFM) for selected fractions revealed a clear increase in aggregate size with buoyant density (see Methods). For a buoyant density of 1.055 g/cm^3, the average height profile was found to be 1.1 ± 0.3 nm, which is consistent with isolated small diameter SWNTs.[20] Average height profiles of 4.3 ± 0.5 and 6.8 ± 0.4 nm were measured for buoyant densities of approximately 1.09 and 1.14 g/cm^3 respectively (Figure 1a). We therefore conclude that the procedure outlined above leads to structural sorting of nanotube aggregates enriched in (6,5) tubes.

Representative absorption and resonant S_2 excitation fluorescence spectra are shown in Figure 1b. The absorption spectra revealed both an increasing red shift of S_1 and non-excitonic visible absorbance with fraction buoyant density. The fluorescence spectra displayed an unexpected negative Stokes shift with respect to the S_1 absorption, while the relative fluorescence quantum yields shown in Figure 1c were found to be reduced monotonically *versus* ρ_b. We found a 50% reduction in emission efficiency for a buoyant density of approximately 1.08 g/cm^3 and at most a reduction of 85% for a buoyant density of 1.15 g/cm^3. In the following sections, we describe how both electrodynamic and excitonic interactions can lead to the observed spectroscopic changes upon aggregation.

Electrodynamic Intertube Interactions. Within a nanotube aggregate, an increase of the dielectric function, ε, relative to an isolated tube can result in a mutual screening of the intratube Coulomb interaction, *W*. In particular, a reduction in the strength of the electron−hole interaction can renormalize the exciton oscillator strength. This effect is well-known in one-dimensional semiconductors where increasing the spatial cutoff of the effective one-dimensional Coulomb interaction, which accounts for screening, can result in a loss of exciton oscillator strength to band-to-band transitions.[21] In carbon nanotubes, the exciton oscillator strength, *f*, has been shown to be proportional to the inverse of the exciton size, L^{-1}, and scales as m^*/ε where m^* is the exciton effective mass.[22]

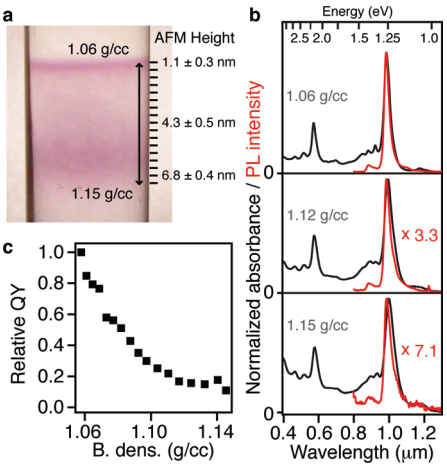

Figure 1. (a) Image of centrifuge vial containing (6,5) enriched nanotubes and nanotube aggregates after 12 h of centrifugation at 207 000*g*. Atomic force microscopy average height profiles of selected fractions are given next to the vial image. (b) Normalized absorption and photoluminescence spectra of selected fractions in (a). (c) Relative fluorescence quantum yields *versus* fraction buoyant density.

The increased response of the free carrier continuum was estimated by calculating the change in the integrated absorbance background underneath the S_2 exciton relative to isolated tubes, defined as $I_{band}/(I_{band} + I_{exc})$ (Figure 2a). A similar analysis was carried out to analyze the effects of external electric fields on free carrier absorption strengths where $I_{band}/(I_{band} + I_{exc})$ was used to estimate the amount of S_1 exciton wave function mixing with the band-to-band continuum.[23] Here it is clear that spectral weight is transferred from S_1 to the absorbance background upon aggregation. We therefore assign the increase in the non-excitonic absorbance to an enhancement of band-to-band or electron−hole pair excitations. This additional absorbance can effectively reduce the absorption cross section of S_2 and possibly provide an efficient route for a pure electronic inter-sub-band relaxation.[11]

Intertube screening can also result in a red shift of the exciton excitation energy, where the dominating effect is a reduction of the free electron−hole pair band gap.[22] However, reductions in the excitation energy have been predicted to be small as compared

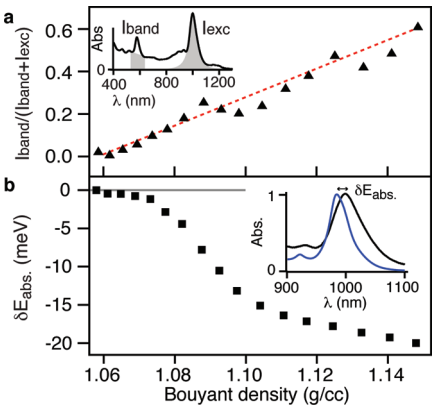

Figure 2. (a) Relative change in the free-carrier oscillator strength near the S_2 exciton as a function of buoyant density. The red line is a guide to the eye, and the inset depicts the areas I_{band} and I_{exc}. (b) Red shift of the S_1 exciton as a function of buoyant density. The inset depicts from where the red shifts were determined.

to reductions in the exciton oscillator strength with increased screening.[24] It has been recently shown that the red shift of the S_1 excitation energy going from one dielectric environment, ε_1, to another, ε_2, in SWNTs can be fit by the following empirical function $\delta E_{abs}(\varepsilon_1,\varepsilon_2) \approx 43(\varepsilon_1^{-1.6} - \varepsilon_2^{-1.6})$ meV.[25] In the case of nanotube aggregation, ε_1 is associated with isolated tubes in solution and ε_2 includes additional effects from neighboring tubes. The magnitude of the dielectric function of (6,5) enriched SWNTs within the frequency range of the S_1 exciton has been experimentally determined to be $\varepsilon_{tube} \approx 5$, emphasizing the limited polarizability of one-dimensional excitons.[26] The effective environmental dielectric constant associated with surfactant-encapsulated SWNTs in water was found to be $\varepsilon_{surf} \approx 3$.[27] From $\delta E_{abs}(\varepsilon_{surf},\varepsilon_{tube})$, we would expect the red shift of S_1 to be approximately 4 meV upon aggregation. As shown in Figure 2b, the S_1 absorption was red-shifted by more than 4 meV for fraction densities greater than 1.08 g/cm^3. Moreover, the fluorescence Stokes shift, defined as the difference of the S_1 absorption and emission energies, is negative, and the emission spectrum can be decomposed into two distinct transitions (Figure 3). Thus, we can not fully explain the observed changes in the optical properties by pure intertube electrodynamic coupling and consider the effects of intertube excitonic coupling in the following sections.

Excitonic Intertube Interactions. The close proximity of neighboring tubes in an aggregate can facilitate tunneling of electrons and holes between tubes which would lead to exciton tunneling and an energetic splitting of the excitation energy. In order to estimate the tunneling strength between a pair of (6,5) nanotubes, we performed an *ab initio* calculation of the electronic levels of a nanotube dimer using the SIESTA code with an intertube wall separation of 3.3 Å. We found that the four-fold degenerate conduction and

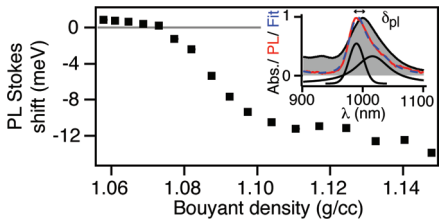

Figure 3. Fluorescence Stokes shift as a function of buoyant density. The inset shows a decomposition of the emission into two distinct peaks.

valence bands were split into doublets separated by 60 and 40 meV, respectively. However, it should be noted that this is an order of magnitude estimate since tunneling is exponentially sensitive to intertube separation, and the tunneling probability was used to give insight on the energetic ordering of the delocalized excitons. Using a Slater−Koster tight-binding model for a dimer with parameters consistent with the SIESTA calculation, the tunneling matrix elements were found to preserve the valley index of the state; that is, an electron or hole at $K^{(\prime)}$ tunnels into an unoccupied electron or hole at the same valley $K^{(\prime)}$. Furthermore, time-reversal symmetry requires the tunneling matrix element from tube A to tube B to be $t^{(m)}_{AB,K} = t^{*(m)}_{AB,K'} = t^{(m)}_R + it^{(m)}_I$, where $m = e(h)$ refers to the conduction (valence) bands of the nanotube. Tubes A and B are identical, and symmetry leads to the results that $|t^{(e)}| \sim 30$ meV and $|t^{(h)}| \sim 20$ meV.

Intratube excitons consist of electrons and holes on the same tube and tunneling of an intratube exciton, with energy $E_{exc,intra} \sim E_g - 350$ meV, where E_g is the quasi-particle gap, can be envisioned as a virtual two-step process where a hole or an electron tunnels from one tube to another followed by the left-over electron or hole tunneling to the other tube, as depicted in Figure 4a. The intermediate state for the tunneling is an intertube exciton with energy $E_{exc,intra} \sim E_g - 200$ meV, where the electron and hole are localized on different tubes of the dimer.[28] The exciton tunneling amplitude is then given by

$$\lambda_{AB,exc,K} \equiv \lambda = -\frac{2t^{(e)}_{AB,K}\, t^{*(h)}_{AB,K}}{E_{exc,inter} - E_{exc,intra}} \qquad (1)$$

where the factor of 2 arises from the ordering of the tunneling of the electron and hole. The hole tunneling factor $t^{*(h)}_{AB,K}$ is conjugated because of the conjugation of the hole wave function in the exciton wave function. In addition to exciton tunneling, there is a red shift of the exciton energy given by

$$\delta E_{A,exc,K} = \delta E_{B,exc,K} = \delta E = -\frac{|t^{(e)}_{AB,K}|^2 + |t^{(h)}_{AB,K}|^2}{E_{exc,inter} - E_{exc,intra}} \qquad (2)$$

Similar results hold for the exciton at K', where $\lambda_{AB,exc,K'} = \lambda^*$. For this specific geometry and phase,

we find $\lambda = \lambda_R + i\lambda_I$, where $\lambda_R \approx -6$ meV, $\lambda_I \approx 1$ meV, and $\delta E \approx -9$ meV.

An alternative mechanism for exciton energy transfer occurs through the Förster interaction. This is represented in the Bethe-Salpeter formalism[29] through the exchange contribution to the Coulomb interaction, which is also responsible for the dark-bright splitting δ_1 of the intratube excitons. The intratube exchange interaction ($\delta_1/2$) has been measured to be approximately 2.5 meV,[30] and for that reason, we expect the intertube exchange interaction to be smaller than the direct tunneling contribution discussed above.

The excitation energies of a dimer can be analyzed by considering an effective Hamiltonian for the excitonically coupled nanotubes, shown schematically in Figure 4b. The spatial extent of the excitons are not affected by λ and δ_1; therefore, the exciton wave function at center-of-mass momentum q can be expanded as $\Psi^{(q)}_{exc}(\mathbf{r}_e,\mathbf{r}_h) = \Sigma_n c^{(q)}_n \int dk A_k u_{n,e,k+q/2}(\mathbf{r}_e) u^*_{n,h,k-q/2}(\mathbf{r}_h)$, where the index $n = K_A$, K'_A, K_B, or K'_B represents the valleys K, K' in the tubes A or B, respectively, and $c^{(q)}_n$ are the coefficients of the expansion. Here, the exciton $\Psi^{(q)}_{exc}$ is expanded in terms of the exciton in each valley n, which in turn is determined by a momentum-dependent amplitude A_k together with the Bloch functions $u_{K,e(h),k}$ of the electrons and holes. The electron(hole) wave functions $u_{n,e(h),k}$ at index n transform under C_2 as $C_2 u_{K,e(h),k} = -u_{K',e(h),k}$ and $C_2 u^*_{K,e(h),k} = u_{K',e(h),-k}$. The expansion for Ψ_{exc} allows us to write an effective 4×4 reduced Hamiltonian at wave-vector q for the coefficients $c^{(q)}_n$ which has the form

$$H(q) = h_0(q) + \begin{pmatrix} \frac{\varepsilon_b(q) - \varepsilon_d(q)}{2}\boldsymbol{\sigma}_x & \boldsymbol{\chi} \\ \boldsymbol{\chi}^* & \frac{\varepsilon_b(q) - \varepsilon_d(q)}{2}\boldsymbol{\sigma}_x \end{pmatrix} \quad (3)$$

where $h_0(q) = (\varepsilon_b(q) + \varepsilon_d(q))/2 + \delta E$ and $\boldsymbol{\chi} = (\lambda_R + \gamma_F)\mathbf{1} + i\lambda_I\boldsymbol{\sigma}_z + \gamma_F\boldsymbol{\sigma}_x$. Here $\varepsilon_{b,d}(q)$ are the dispersions of the bright and dark intratube excitons, $\gamma_F > 0$ is the strength of the intertube Förster interaction, $\mathbf{1}$ is the 2×2 identity, and $\boldsymbol{\sigma}_{x,z}$ are the 2×2 Pauli matrices. The diagonal elements of the Hamiltonian, H_{11} and H_{22}, are intratube mixing of excitons at K and K' of $(\varepsilon_b(q) - \varepsilon_d(q))/2$, which for $q = 0$ is the exchange splitting $\delta_1/2$. The off-diagonal elements, H_{21} and H_{12}, are both intertube exciton tunneling of strength $\lambda_R + i\lambda_I$ and the Förster interaction γ_F at valleys K' and K, respectively.

Ignoring the Förster interaction ($\gamma_F = 0$) and considering only excitons with $q = 0$, shown schematically in Figure 4b, the diagonalization of H leads to two partially bright states with energies $E_{b\pm} = h_0(0) \pm |\xi|$ and oscillator strengths proportional to $f\pm = |1 \pm \xi/|\xi||^2$, where $\xi = \delta_1/2 + \lambda$. There is also a pair of dark states with energies given by $E_{d\pm} = h_0(0) \pm |\xi_1|$, where $\xi_1 = \lambda - \delta_1/2$. The delocalized dimer excitons are labeled in energetic order as d+, b+, b−, and d−. From our estimates of λ and δ_1, we would expect a two peaked absorption spectrum with the upper and lower bright states having energies and oscillator strengths of $E_{b+} = -8$ meV, $f_+ = 0.2$, and $E_{b-} = -15$ meV, $f_- = 1.8$, respectively. Here the excitation energies are relative to the isolated tube bright state A_2 (Figure 4c), and the total oscillator strengths are defined such that $f = 1$ for a monomer and $\sum f = 2$ for a dimer. The dipole forbidden excitons would have energies of $E_{d+} = -3$ meV and $E_{d-} = -20$ meV. If we consider Förster coupling to be the dominant mechanism of exciton delocalization ($\lambda = 0$), then the excitation spectra would be that of an H-type molecular aggregate.[31] Specifically, if we assume $\gamma_F = \delta_1/2$ and δE is equal to what is the expected red shift of the excitation energy by electrodynamic effects, we find a single bright exciton with an energy of $E_b = 1$ meV relative to A_2 (Figure 4c).

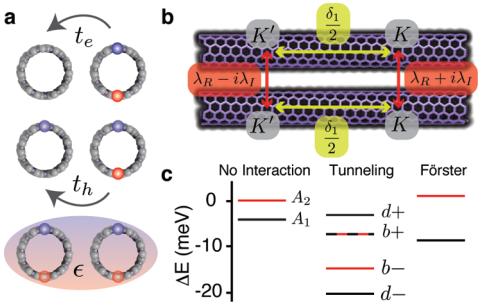

Figure 4. (a) Schematic of the virtual two-step exciton tunneling process in a nanotube dimer *via* an intertube exciton intermediate state. Mutual intertube screening by the dielectric function ε is depicted in the shaded region. (b) Schematic of the Hamiltonian representing the intratube exchange splitting δ_1 and the intertube tunneling induced splitting λ. (c) Exciton energies for a monomer and a dimer. The isolated tube levels are labeled by their C_2 symmetry[9] and the dimers by their respective optical activities and energy. The limits of pure exciton tunneling and Förster exciton energy transfer are shown for comparison.

From the above discussion, it is clear that the absorbance will be dominated by the lower energy partially bright exciton in the event of intertube exciton tunneling. Moreover, the excitation energy of this state can account for the large red shifts of S_1 in Figure 2b not accounted for by electrodynamic effects. Indeed, if we extend the Hamiltonian in eq 3 to three excitonically coupled tubes, we find as in the case of the dimer there is an upper weakly dipole allowed state and a lower strongly dipole allowed state that is further red-shifted from A_2 (see Methods for details). Nonetheless, the fluorescence lifetime in SWNTs is dominated by nonradiative decay and can be described by diffusion-limited contact quenching of excitons in the limit of relatively low fluorescence quantum yields.[32] Thus, the fluorescence lifetime and the nature of delocalized exciton diffusion are discussed in the following section to understand the peculiar spectral splitting of the S_1 emission.

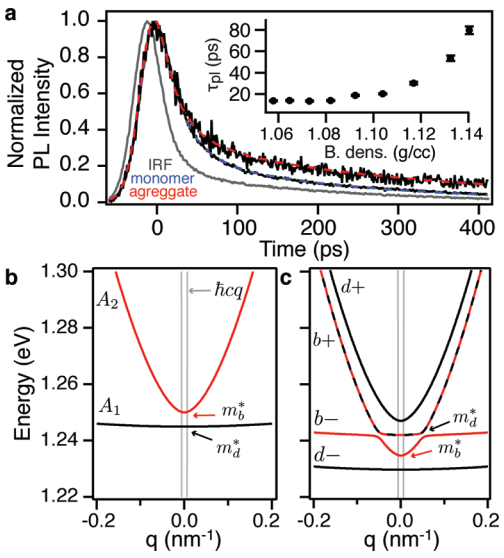

Figure 5. (a) Normalized fluorescence intensity and fit functions (red and blue dashed lines) for selected fractions. The gray trace is the instrument response function (IRF). The inset shows the average photoluminescence lifetimes with error bars associated with the double exponential fit described in the text. (b) Exciton dispersions for the bright A_2 and dark A_1 intratube excitons with effective masses m_b^* and m_d^*, respectively. The gray lines indicate the dispersion of light of speed c. (c) Exciton dispersions for the four delocalized dimer excitons calculated from the Hamiltonian in eq 3, where the weakly dipole allowed b+ exciton and the strongly dipole allowed b− exciton have effective masses of m_d^* and m_b^*, respectively, near $q = 0$. The lower state b− dominates the absorption spectrum, while the upper state b+ dominates the emission spectrum because of the strong dependence of the fluorescence lifetime on the diffusion constant.

Diffusion-Limited Exciton Lifetimes and Quantum Yields. Fluorescence lifetimes were measured by time correlated single photon counting, where the samples were excited at 400 nm with $\approx 5 \times 10^{12}$ photons/cm^2. The emission was collected through a 950 nm low pass filter such that the total photons counted included the entire (6,5) emission spectrum. As shown in Figure 5a, the normalized fluorescence decay displays a clear increase of fluorescence lifetime with increasing buoyant density. The dynamics of the fluorescence decay was fit with a double exponential, $I(t) = (C_1 e^{-(t/\tau_1)} + C_2 e^{-(t/\tau_2)})/(C_1 + C_2)$, and the average fluorescence lifetimes were computed as $\tau_{pl} = \int_0^\infty I(t)dt$. As shown in the inset of Figure 5a, τ_{pl} increases monotonically from ~14 ps for isolated tubes to ~80 ps for the fractions with the largest buoyant density.

In the previous section, we have shown that the higher energy bright exciton b+ has a smaller oscillator strength than the lower energy bright exciton b−, and therefore b− dominates the absorption spectrum. However, for b+ to dominate the emission spectrum, the fluorescence decay rate k_{pl+} must be smaller than k_{pl-} and scattering between the states must be negligible. The assumption that there is insignificant scattering between different parity states is validated by a recent discovery of a non-equilibrium distribution between intratube bright and dark excitons.[33] Therefore, the negative Stokes shift can be understood by considering the ratio of the time average within a period T of the number of photons emitted by both states $\bar{N}_+/\bar{N}_- = [(1/T)\int_0^T N_+^0 e^{-k_{pl+}t}dt)]/[(1/T)\int_0^T N_-^0 e^{-k_{pl-}t}dt)]$, where $k_\pm$ and $N_\pm^0$ are the effective fluorescence decay rates and initial populations of the upper and lower bright excitons, respectively. If we assume that $N_-^0 \approx N_+^0$ upon inter-sub-band decay from S_2, then within a time period longer than the decay times $\bar{N}_+/\bar{N}_- \approx k_{pl-}/k_{pl+} = \tau_{pl+}/\tau_{pl-}$. Within the model of one-dimensional exciton diffusion-limited contact quenching, the fluorescence lifetime is defined as

$$\tau_{pl} = \frac{\pi}{2(d_q^{-1} + l^{-1})^2 D} \quad (4)$$

where d_q is the average quenching site distance, l is the nanotube length, and D is the exciton diffusion constant.[32] The ratio of the number of photons emitted by each state reduces to $\bar{N}_+/\bar{N}_- \approx D_-/D_+$, and the diffusion constant of the lower state b− must be much larger than the diffusion constant of the upper state b+ for a negative Stokes shift to occur.

The diffusion constant for a parabolic exciton band, near $q = 0$, can be expressed in terms of the dephasing time τ_s and the effective mass m^* such that

$$D = \frac{\tau_s k_B T}{m^*} \quad (5)$$

In order to determine the effective masses of each delocalized state, we diagonalized H in eq 3 with full q dependence. The dispersion of the A_2 intratube bright exciton $\varepsilon_b(q)$ was adapted from a recent Bethe-Salpeter calculation of the excitonic properties of (6,5) carbon nanotubes where the effective mass was found to be $m_b^* \approx 0.1 m_e$.[34] The A_1 dark intratube exciton was assumed to have a dispersion of a free electron with an effective mass of $m_d^* = 1.5 m_e$[35] (Figure 5b). As shown in Figure 5c near $q = 0$, the upper bright state b+ has a dispersion equal to the dark exciton A_1 and the lower bright state b− has a dispersion equal to the bright exciton A_2. Only excitons with a wave-vector less than or equal to $\varepsilon_c/\hbar c$, where ε_c is the photon energy and c is the speed of light, can couple to the light field. As a result, we restricted our analysis to the band minimum at $\varepsilon_{b+,b-}(0)$. In turn, the effective mass of b+ near $q = 0$ is approximately m_d^* and the effective mass of b− is approximately m_b^*. Similar results hold for the excitonically coupled SWNT trimer (Figure 8). When the dephasing times of the two optically active states are similar $\tau_{s+} \approx \tau_{s-}$, it is clear that the upper state will have a diffusion constant at least an order of magnitude smaller than the lower state $D_+ \ll D_-$ and dominate the emission spectrum.

We now describe the origin of the observed reductions of the fluorescence quantum yields upon aggregation in Figure 1c using the fluorescence lifetime in

eq 4. By dividing τ_{pl} by the radiative lifetime τ_r, the fluorescence quantum yield can be determined as a function of average quenching site distance d_q^{-1} as

$$\Phi = \frac{\pi}{2(d_q^{-1} + l^{-1})^2 D\tau_r} \quad (6)$$

Lefebrve and Finnie reported that the average emission efficiency of a dimer of semiconducting SWNTs was reduced by ≈50% relative to a monomer and attributed this effect to additional nonradiative losses due to the doubling of the number of exciton quenching defects.[14] This was rationalized by an apparent thermal equilibrium between upper and lower energy exciton states in nanotube dimers coupled by the Förster interaction made up of different chirality tubes. However, at any instance of incoherent exciton transfer, the exciton is localized on one tube and the defect density experienced would be that of an isolated tube. In the case of coherent delocalization, the overall defect density would be the sum of the two tubes' defect densities before aggregation.

Isolated (6,5) CoMoCat tubes with quantum yields of ≈1.3% were found to have radiative lifetimes, diffusion constants, and defect distances of $\tau_r \approx 1.6$ ns, $D \approx 11$ cm^2 s^{-1}, and $d_q \approx 120$ nm, respectively.[32] Here, the dimer would have twice as many defects as the monomer $d_q \approx 60$ nm, and using the fact that $\tau_r \propto f^{-1}$, the upper b+ and lower b− states would have radiative lifetimes of $\tau_{r+} \approx 0.9$ ns and $\tau_{r-} \approx 8$ ns. The diffusion constants of b+ and b− would be on the order of $D_+ \approx 1$ cm^2 s^{-1} and $D_- \approx 11$ cm^2 s^{-1}, respectively, accounting for the effective mass in eq 5. Using eq 6, we find the quantum yields in the limit of long tubes, $l^{-1} \approx 0$, of each dimer state are $\Phi_+ \approx 0.6\%$ and $\Phi_- \approx 0.7\%$. By considering three excitonically coupled tubes, the quantum yields would clearly be further reduced as d_q would become smaller. Thus, simultaneous reductions in the emission efficiency and long-lived, negative Stokes shifted emission in SWNT aggregates are captured by delocalized excitons undergoing diffusion-limited contact quenching.

CONCLUSION

In summary, the optical properties of nearly pure chirality semiconducting single-wall carbon nanotube aggregates display strong deviations from isolated tubes. This work calls for a re-evaluation of how we describe intertube interactions in the context of optical properties and energy transport. The origin of this behavior is demonstrated and quantified as resulting from simultaneous electrodynamic and excitonic intertube interactions. Screening of the intratube Coulomb interaction is found to manifest itself as an increase of the oscillator strength of continuum excitations at expense of the S_1 exciton. However, the majority of the changes of the aggregate optical properties relative to isolated tubes are well described by coherent exciton delocalization. Our theoretical model predicts a tunneling induced splitting of the degenerate intratube conduction and valence bands that ultimately lead to delocalized excitons. Incoherent Förster exciton energy transfer is predicted to be energetically unfavorable as the exchange energy is smaller than the direct tunneling energy. Two of the delocalized excitons are found to be optically active, with the higher and lower energy states having relatively small and large oscillator strengths with $q \approx 0$ effective masses of intratube dark and bright excitons, respectively. Long-lived, negative Stokes shifted photoluminescence suggests that as in low fluorescence quantum yield isolated tubes the photoluminescence decay in aggregates is dominated by exciton diffusion-limited contact quenching whose dynamics depend strongly on effective mass.

Beyond the observed effects on the absorption and fluorescence spectra, the importance of coherent exciton energy transfer should be considered for other aspects of nanotube photophysics. Potential consequences include a re-evaluation of microscopic scattering mechanisms such as exciton−phonon coupling in nanotube aggregates[36] and the possibility of realizing microscale quantum light sources taking advantage of delocalized rather than localized excitons.[37] Moreover, the observed monotonic changes in the optical properties as a function of buoyant density suggest some degree of structural sorting by oligomer size. In the context of molecular states, specifically designed nanotube aggregates or artificial molecules can be designed with selective aggregation and density gradient ultracentrifugation as preparative tools. As a result, investigating exciton delocalization in engineered carbon nanotube aggregates may provide model systems for coherent energy transport in natural light-harvesting systems.[38,39] Finally, our findings emphasize the important role pure chirality samples have in discovering new electronic and optical properties that are beyond the single carbon nanotube intrinsic limit.

METHODS

Selective Aggregation and Fractionation of (6,5) Enriched Aggregates. Nanotube suspensions were prepared by isopycnic fractionation of surfactant-encapsulated (6,5) enriched SWeNT SG 65 (SouthWest NanoTechnologies) material. Here, raw soot is dispersed in 2 wt % aqueous sodium cholate (SC) by ultrasonication for 2 h using a Branson 450 horn sonifer at a duty cycle of 30% and output power of 3. In order to remove insoluble

material and concentrate the suspension, 5 mL of the resulting mixture was centrifuged for 7.5 h at 41 krpm with a 7 mL step gradient of 100% OptiPrep with 2 wt % SC in a Sorvall centrifuge with a TV-640 swinging bucket rotor. The concentrated supernatant was fractionated using a home-built upward displacement fractionator using Fluorinert FC-40 as a displacement medium. Density differentiation of the supernatant was carried out by using sodium dodecyl sulfate (SDS) as a co-surfactant to SC in the density gradient at a ratio of 1:4. A step gradient was formed consisting of five layers with 100, 50, 32.5, 25, and 0% OptiPrep and 2 wt % of aqueous co-surfactant. The concentrated supernatant was mixed in the 32.5% OptiPrep layer. The centrifuge vial was capped and tilted horizontally for 2 h to form a linear gradient. The linear gradient was then centrifuged for 12 h at 41 krpm, which resulted in colored bands signifying structural sorting. Only the topmost violet fractions were collected.

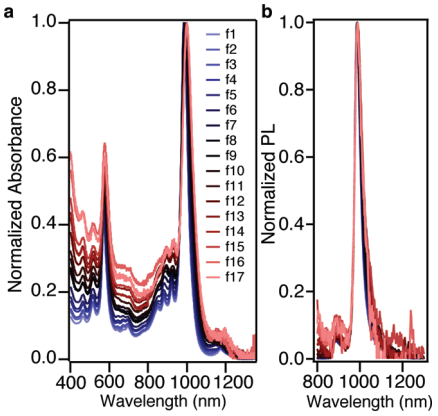

Figure 6. Spectra from all fractions collected in Figure 1a.

The composition of the starting material used to make the aggregates in this investigation was estimated by calculating the first derivative of the absorption spectra and comparing the relative amplitudes of each (*n*,*m*) species' first exciton transition. We found at least 85% of the starting material was composed of the (6,5) tube, which is consistent with previous studies.[18]

In order to make (6,5) enriched aggregates, approximately 1 mL of (6,5) enriched material was placed in 3.5 kDa dialysis tubing (Sigma Aldrich) and submerged in 100 mL of HPLC water for 24 h. Upon flocculation, the tubes were resuspended in 2% SC by mild sonication. The suspension was then structurally sorted by density gradient ultracentrifugation with the same procedure above except only 2% SC was used as the surfactant. Fractions were collected at a volume of 150 μL and ranged in density from 1.058 to 1.148 g/cm^3. The absorption spectra of all fractions are shown in Figure 6.

Aggregate Size Characterization. In brief, samples were prepared for tapping mode AFM by spin-coating selected fractions on cleaved mica. Details on the exact sample preparation can be found elsewhere.[40] Images are shown in Figure 7 and show a clear increase in aggregate size as a function of buoyant density.

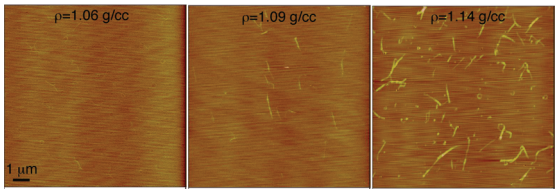

Figure 7. Atomic force microscopy images from selected fractions in Figure 1a.

Exciton Tunneling Model for More than Two Tubes. The Hamiltonian in eq 3 of the main text may be extended to more than two tubes by adding intratube terms H_{ij} to the diagonal and intertube terms H_{ij} and H_{ji} to the off-diagonals. However, the tunneling energy $\lambda_R + i\lambda_I$ is exponentially sensitive to intertube separation and must be accounted for. In the case of three tubes, the tunneling energy is approximately the same as a dimer because the structure is trigonal planar, and the delocalized excitons are nearly the same except for two additional dark states (Figure 8).

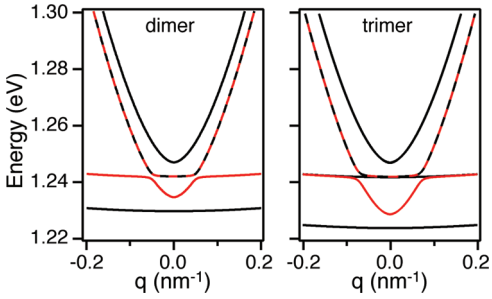

Figure 8. Comparison of the states calculated from eq 3 (left) and eq 3 extended to three excitonically coupled tubes (right).

Acknowledgment. J.C. thanks Tobias Hertel for generous support as well as Timo Hefner and Dominik G. Stich for technical assistance. J.S. thanks JQI-NSF-PFC, DARPA-QUEST, and LPS-NSA. M.L.C. acknowledges the NSF Grant DMR07-05941 and Director, Office of Science, Basic Energy Sciences, Materials Sciences and Engineering Division of the U.S. Department of Energy under Contract No. DE-AC02-05CH11231. This work was performed, in part, at the Center for Integrated Nanotechnologies, a U.S. Department of Energy, Office of Basic Energy Sciences user facility and partially supported by LANL-LDRD program. Los Alamos National Laboratory is operated by Los Alamos National Security, LLC, for the National Nuclear Security Administration of the U.S. Department of Energy under Contract DE-AC52-06NA25396.

REFERENCES AND NOTES

1. Adams, D. M.; Brus, L.; Chidsey, C. E. D.; Creager, S.; Creutz, C.; Kagan, C. R.; Kamat, P. V.; Lieberman, M.; Lindsay, S.; Marcus, R. A.; *et al.*Charge Transfer on the Nanoscale: Current Status. *J. Phys. Chem. B* **2003,** *107*, 6668–6697.
2. Gust, D.; Moore, T. A.; Moore, A. L. Mimicking Photosynthetic Solar Energy Transduction. *Acc. Chem. Res.* **2001,** *34*, 40–48.
3. Baughman, R. H.; Zakhidov, A. A.; de Heer, W. A. Carbon Nanotubes—The Route toward Applications. *Science* **2002,** *297*, 787–792.
4. Geim, A. K.; Novoselov, K. S. The Rise of Graphene. *Nat. Mater.* **2007,** *6*, 183–191.
5. Capaz, R. B.; Spataru, C. D.; Ismail-Beigi, S.; Louie, S. G. Diameter and Chirality Dependence of Exciton Properties in Carbon Nanotubes. *Phys. Rev. B* **2006,** *74*, 121401.
6. Yang, L.; Deslippe, J.; Park, C.-H.; Cohen, M. L.; Louie, S. G. Excitonic Effects on the Optical Response of Graphene and Bilayer Graphene. *Phys. Rev. Lett.* **2009,** *103*, 186802.
7. Wang, F.; Dukovic, G.; Brus, L. E.; Heinz, T. F. The Optical Resonances in Carbon Nanotubes Arise from Excitons. *Science* **2005,** *308*, 838–841.
8. Lüer, L.; Hoseinkhani, S.; Polli, D.; Crochet, J.; Hertel, T.; Lanzani, G. Size and Mobility of Excitons in (6,5) Carbon Nanotubes. *Nat. Phys.* **2009,** *5*, 54–58.
9. Barros, E. B.; Capaz, R. B.; Jorio, A.; Samsonidze, G. G.; Filho, A. G. S.; Ismail-Beigi, S.; Spataru, C. D.; Louie, S. G.; Dresselhaus, G.; Dresselhaus, M. S. Selection Rules for One- and Two-Photon Absorption by Excitons in Carbon Nanotubes. *Phys. Rev. B* **2006,** *73*, 241406.
10. Avouris, P.; Freitag, M.; Perebeinos, V. Carbon-Nanotube Photonics and Optoelectronics. *Nat. Photonics* **2008,** *2*, 341–350.
11. Hertel, T.; Perebeinos, V.; Crochet, J.; Arnold, K.; Kappes, M.; Avouris, P. Intersubband Decay of 1-D Exciton Resonances in Carbon Nanotubes. *Nano Lett.* **2008,** *8*, 87–91.

12. Crochet, J.; Clemens, M.; Hertel, T. Quantum Yield Heterogeneities of Aqueous Single-Wall Carbon Nanotube Suspensions. *J. Am. Chem. Soc.* **2007,** *129*, 8058–8059.
13. Tan, P. H.; Rozhin, A. G.; Hasan, T.; Hu, P.; Scardaci, V.; Milne, W. I.; Ferrari, A. C. Photoluminescence Spectroscopy of Carbon Nanotube Bundles: Evidence for Exciton Energy Transfer. *Phys. Rev. Lett.* **2007,** *99*, 137402.
14. Lefebvre, J.; Finnie, P. Photoluminescence and Förster Resonance Energy Transfer in Elemental Bundles of Single-Walled Carbon Nanotubes. *J. Phys. Chem. C* **2009,** *113*, 7536–7540.
15. Wong, C. Y.; Curutchet, C.; Tretiak, S.; Scholes, G. D. Ideal Dipole Approximation Fails To Predict Electronic Coupling and Energy Transfer between Semiconducting Single-Wall Carbon Nanotubes. *J. Chem. Phys.* **2009,** *130*, 081104.
16. Lüer, L.; Crochet, J.; Hertel, T.; Cerullo, G.; Lanzani, G. Ultrafast Excitation Energy Transfer in Small Semiconducting Carbon Nanotube Aggregates. *ACS Nano* **2010,** *4*, 4265–4273.
17. Wang, F.; Sfeir, M. Y.; Huang, L.; Huang, X. M. H.; Wu, Y.; Kim, J.; Hone, J.; O'Brien, S.; Brus, L. E.; Heinz, T. F. Interactions between Individual Carbon Nanotubes Studied by Rayleigh Scattering Spectroscopy. *Phys. Rev. Lett.* **2006,** *96*, 167401.
18. Arnold, M. S.; Green, A. A.; Hulvat, J. F.; Stupp, S. I.; Hersam, M. C. Sorting Carbon Nanotubes by Electronic Structure Using Density Differentiation. *Nat. Nanotechnol.* **2006,** *1*, 60–65.
19. Crochet, J.; Clemens, M.; Hertel, T. Optical Properties of Structurally Sorted Single-Wall Carbon Nanotube Ensembles. *Phys. Status Solidi B* **2007,** *244*, 3964–3968.
20. Naumov, A. V.; Kuznetsov, O. A.; Harutyunyan, A. R.; Green, A. A.; Hersam, M. C.; Resasco, D. E.; Nikolaev, P. N.; Weisman, R. B. Quantifying the Semiconducting Fraction in Single-Walled Carbon Nanotube Samples through Comparative Atomic Force and Photoluminescence Microscopies. *Nano Lett.* **2009,** *9*, 3203–3208.
21. Ogawa, T.; Takagahara, T. Optical Absorption and Sommerfeld Factors of One-Dimensional Semiconductors: An Exact Treatment of Excitonic Effects. *Phys. Rev. B* **1991,** *44*, 8138–8156.
22. Perebeinos, V.; Tersoff, J.; Avouris, P. Scaling of Excitons in Carbon Nanotubes. *Phys. Rev. Lett.* **2004,** *92*, 257402.
23. Perebeinos, V.; Avouris, P. Exciton Ionization, Franz-Keldysh, and Stark Effects in Carbon Nanotubes. *Nano Lett.* **2007,** *7*, 609–613.
24. Ando, T. Environment Effects on Excitons in Semiconducting Carbon Nanotubes. *J. Phys. Soc. Jpn.* **2010,** *79*, 024706.
25. Ohno, Y.; Maruyama, S.; Mizutani, T. Environmental Effects on Photoluminescence of Single- Walled Carbon Nanotubes, Carbon Nanotubes. *INTECH*, 2010.
26. Fagan, J. A.; Simpson, J. R.; Landi, B. J.; Richter, L. J.; Mandelbaum, I.; Bajpai, V.; Ho, D. L.; Raffaelle, R.; Walker, A. R. H.; Bauer, B. J.; *et al.* Dielectric Response of Aligned Semiconducting Single-Wall Nanotubes. *Phys. Rev. Lett.* **2007,** *98*, 147402.
27. Capaz, R. B.; Spataru, C. D.; Ismail-Beigi, S.; Louie, S. G. Excitons in Carbon Nanotubes: Diameter and Chirality Trends. *Phys. Status Solidi B* **2007,** *244*, 4016–4020.
28. Sau, J. D.; Cohen, M. L. Possible Electric-Field-Induced One-Dimensional Excitonic Insulators in Pairs of Carbon Nanotubes. *Phys. Rev. B* **2008,** *78*, 115436.
29. Spataru, C. D.; Ismail-Beigi, S.; Benedict, L. X.; Louie, S. G. Excitonic Effects and Optical Spectra of Single-Walled Carbon Nanotubes. *Phys. Rev. Lett.* **2004,** *92*, 077402.
30. Shaver, J.; Crooker, S. A.; Fagan, J. A.; Hobbie, E. K.; Ubrig, N.; Portugall, O.; Perebeinos, V.; Avouris, P.; Kono, J. Magneto-optical Spectroscopy of Highly Aligned Carbon Nanotubes: Identifying the Role of Threading Magnetic Flux. *Phys. Rev. B* **2008,** *78*, 081402.
31. Kasha, M. Energy Transfer Mechanisms and the Molecular Exciton Model for Molecular Aggregates. *Radiat. Res.* **1963,** *20*, 55–71.
32. Hertel, T.; Himmelein, S.; Ackermann, T.; Stich, D.; Crochet, J. Diffusion Limited Photoluminescence Quantum Yields in 1-D Semiconductors: Single-Wall Carbon Nanotubes. *ACS Nano* **2010,** *4*, 7161–7168.
33. Matsunaga, R.; Miyauchi, Y.; Matsuda, K.; Kanemitsu, Y. Symmetry-Induced Nonequilibrium Distributions of Bright and Dark Exciton States in Single Carbon Nanotubes. *Phys. Rev. B* **2009,** *80*, 115436.
34. Jiang, J.; Saito, R.; Samsonidze, G. G.; Jorio, A.; Chou, S. G.; Dresselhaus, G.; Dresselhaus, M. S. Chirality Dependence of Exciton Effects in Single-Wall Carbon Nanotubes: Tight-Binding Model. *Phys. Rev. B* **2007,** *75*, 035407.
35. Perebeinos, V.; Tersoff, J.; Avouris, P. Radiative Lifetime of Excitons in Carbon Nanotubes. *Nano Lett.* **2005,** *5*, 2495–2499.
36. Luo, Z.; Papadimitrakopoulos, F.; Doorn, S. K. Bundling Effects on the Intensities of Second-Order Raman Modes in Semiconducting Single-Walled Carbon Nanotubes. *Phys. Rev. B* **2008,** *77*, 035421.
37. Högele, A.; Galland, C.; Winger, M.; Imamoglu, A. Photon Antibunching in the Photoluminescence Spectra of a Single Carbon Nanotube. *Phys. Rev. Lett.* **2008,** *100*, 217401.
38. Brixner, T.; Stenger, J.; Vaswani, H.; Cho, M.; Blankenship, R.; Fleming, G. Two-Dimensional Spectroscopy of Electronic Couplings in Photosynthesis. *Nature* **2005,** *434*, 625–628.
39. Collini, E.; Wong, C. Y.; Wilk, K. E.; Curmi, P. M. G.; Brumer, P.; Scholes, G. D. Coherently Wired Light-Harvesting in Photosynthetic Marine Algae at Ambient Temperature. *Nature* **2010,** *463*, 644–U69.
40. Duque, J. G.; Pasquali, M.; Schmidt, H. K. Antenna Chemistry with Metallic Single-Walled Carbon Nanotubes. *J. Am. Chem. Soc.* **2008,** *130*, 15340–15347.